Seismic monitoring of Séchilienne rockslide (French Alps): Analysis of seismic signals and their correlation with rainfalls

Agnès Helmstetter[1] and Stéphane Garambois[1]

Received 14 September 2009; revised 22 December 2009; accepted 4 February 2010; published 4 August 2010.

[1] In the French Alps, Séchilienne rockslide is one of the natural phenomena that presents one of the highest levels of risk in terms of socioeconomical outcomes. This rockslide has been active for a few decades and has been instrumented since 1985. The current very active volume of this rockslide is estimated to be up to 5 million m^3, located on the border of a slowly moving mass reaching 50–100 million m^3. The velocity of the most active zone reached 1.4 m/yr in 2008, about twice the value of 2000. A seismic network was installed on this rockslide in May 2007 to supplement the monitoring system. It has now recorded several thousand events, mostly rockfalls but also hundreds of local and regional earthquakes, which can be distinguished and classified from their signal characteristics. Rockfalls and microseismicity, which occur in bursts of activity, are found to be weakly, but significantly, correlated with rainfall. Rockfall occurrence increases linearly with precipitation, with however strong fluctuations of the numbers of rockfalls per day for the same rainfall intensity. No threshold was found for rainfall triggering, with even 1 mm of rain being enough to trigger rockfalls. Rockfall activity starts almost immediately during a rainfall episode and lasts for several days after the rainfall. Rain also induces strong accelerations of the rockslide movement, which also start quasi-instantaneously and last for about a month.

Citation: Helmstetter, A., and S. Garambois (2010), Seismic monitoring of Séchilienne rockslide (French Alps): Analysis of seismic signals and their correlation with rainfalls, *J. Geophys. Res.*, *115*, F03016, doi:10.1029/2009JF001532.

1. Introduction

[2] Landslides can be triggered by many different causes, including intense or extended rainfall and earthquakes. Understanding of the mechanisms influencing landslide dynamics is limited by the lack of dense and multiparameter data, as very few active rockslides are nowadays instrumented with continuous measurements. Although there exists an extensive literature about the triggering of shallow landslides or rockfalls by rainfall (see *Guzzetti et al.* [2007] for a recent review), the catalogs used in these studies often exhibit imprecise times (about 1 day), because they were generally constructed from discrete field observations or aerial and satellite images. In contrast, seismic monitoring presents the opportunity to study the triggering mechanisms of landslides with very precise event times, but in a small area. This method is also highly sensitive, allowing one to record several thousand events per year. Finally, seismometers also detect microearthquakes induced by the slope movement and by fracturing of the rock mass, in addition to those generated by debris flows and rockfalls. Seismology thus appears to be a promising technique to complement classical techniques for landslide monitoring.

[3] Local seismological networks have been occasionally used for monitoring active landslides. Most seismological studies have used regional networks, primarily dedicated to monitor seismicity [*McSaveney and Downes*, 2002]. Seismology has been used for studying landslide propagation, detecting precursory signals, or analyzing site effects. *Norris* [1994] used seismic stations to detect rock avalanches at three Cascade Range volcanoes. *McSaveney* [2002] and *McSaveney and Downes* [2002] estimated the onset time, duration, volume and propagation velocity of rockfall avalanches in New Zealand from seismic signals. *Deparis et al.* [2008] investigated ten rockfalls recorded in the French Alps by a regional seismic network and tried to link seismic parameters to rockfall properties. *Brodsky et al.* [2003] used seismic waves to characterize landslide basal friction for three huge landslides. *Del Gaudio et al.* [2008] analyzed seismic site amplification from microtremors in a landslide prone area (central Italy). Permanent networks were also installed in Norway on the Åknes landslide [*Roth et al.*, 2006] and in Swiss Alps on the Randa landslide [*Spillmann et al.*, 2007] in order to characterize microseismicity of these active rockslides. At a smaller scale, *Amitrano et al.* [2005] observed precursory microseismicity before a cliff collapse in Normandy (France).

[4] In this study, we present the results obtained from the seismic monitoring of a large active rockslide. In the French Alps, Séchilienne rockslide presents one of the highest levels of risk in terms of socioeconomical outcomes. The failure of

[1]Laboratoire de Géophysique Interne et Tectonophysique, Université Joseph Fourier, CNRS, Grenoble, France.

0148-0227/10/2009JF001532

this landslide (3 to several tens of millions m^3) is likely to form a natural dam which could potentially block the Romanche River located just bellow [*Panet*, 2000]. Its subsequent rupture would have devastating consequences downstream for people and facilities. For these reasons, this area has been extensively instrumented since 1988 for surveillance purposes using a multitechniques displacement network (noncontinuous GPS, laser, radar, extensometers) and a meteorological station.

[5] In May 2007, this monitoring system was supplemented with a seismological network. The main objective is to detect microseismicity activity associated with fractures within the rock mass and/or rockfalls occurring within the rockslide, and to characterize these events (location, magnitude and mechanisms of microearthquakes, volume and propagation velocity of rockfalls). This network also allows study of small local earthquakes generated by the nearby Belledonne Border fault [*Thouvenot et al.*, 2003], and characterization of the properties and heterogeneities of seismic site amplification of the landslide. It will also permit seismic noise analyses to monitor very weak temporal changes in seismic wave velocities between each sensor due to fracture openings or fluid flow.

[6] In less than 2 years, several thousands seismic events have been recorded. In this paper, we first focus on the various types of signals which were acquired and on their characteristics. Most events have been identified as rockfalls, but hundreds of microearthquakes and distant earthquakes have also been detected. The microseismicity and rockfall activity appear very variable, from zero to more than 100 events per day during seismic crises. Most of these peaks are correlated with rainfall and are also associated with accelerations of the movement.

[7] Landslides triggered by rainfall are generally caused by the buildup of subsurface water pressure. Many investigations on rainfall-induced landslides have attempted to estimate minimum thresholds for initiation of landslides [*Guzzetti et al.*, 2007]. Our monitoring network gives us the opportunity to investigate the relation between rockfalls and rainfall, using a large data set of events with very accurate times. This study suggests the absence of any triggering threshold, and also allows us to analyze the time delay between rainfall, rockfall activity and slope movement dynamics.

2. Séchilienne Rockslide

[8] The Séchilienne landslide is located in the southwestern Belledonne massif, one of the Paleozoic external crystalline massifs of the French Alps, which is divided in two major tectonic blocks: the external domain to the west and the internal one to the east. These two blocks are separated by a major Late Paleozoic subvertical fault, known as the Belledonne Middle Fault. The southern part of the Belledonne massif is deeply incised by the east-west striking lower Romanche River valley (Figure 1). This incision results from the alternate activity of the Romanche River and the Romanche glacier, which developed repeatedly during the Quaternary glaciations [*Montjuvent and Winistorfer*, 1980]. The resulting morphology displays very steep slopes, around 35° to 40°, which are affected by large active or past gravitational movements in the micaschists. Eight major landslides have been reported in the area, including the large Séchilienne landslide which is affecting the south facing valley flank of the Romanche River.

[9] In the Séchilienne area, the valley slope consists mainly of micaschists with interbedded quartz-feldspar-rich layers, which were affected by both the Hercynian and Alpine orogenies. Due to this tectonic history, the micaschist bedrock is cut by several faults and three sets of near-vertical fractures [*Pothérat and Alfonsi*, 2001]. The global geometry of the hill displays a nested slide delimited at the top by a 20 to 40 m high scarp (the Mont-Sec scarp). This scarp presents a corner shape on the northeast limit of the landslide, and extents several hundred meters to the west and a few hundred of meters to the south. It was studied using cosmic ray exposure dating to provide chronological constraints on the failure time and kinematics [*Le Roux et al.*, 2009]. The part of the slope that exhibits more signs of current instability (high-motion zone; Figure 2) is located in the middle of the hill at an elevation of 600–900 m, and involves a rock volume estimated from geometric constraints to be about 3 to 5 million m^3 [*Giraud et al.*, 1990].

[10] Sismalp seismological network has shown a concentration of seismic sources along a strip which is parallel to the western edge of the Belledonne massif [*Thouvenot et al.*, 2003] and extends for more than 50 kilometers. Earthquakes are located at depths shallower than 10 km and focal solutions reveal a dextral strike-slip seismotectonic regime. Since the installation of Sismalp network in 1989, the largest event detected on this fault is a $m_l = 3.5$ earthquake, which occurred in 1999 only 7 km southwest of Séchilienne.

[11] The rockslide has been extensively instrumented and studied since 1988 thanks to the presence of a displacement monitoring system designed for surveillance and alert purposes [*Evrard et al.*, 1990; *Duranthon et al.*, 2003]. This instrumentation was supplemented by modeling computations [*Vengeon et al.*, 1999; *Pothérat and Alfonsi*, 2001] and hydrological [*Guglielmi et al.*, 2002] and geophysical studies [*Méric et al.*, 2005]. In 1993–1994, a 240 m long gallery was excavated at an elevation of 710 m in a zone located to the west of the high-motion zone (Figure 2) characterized by a displacement rate of about 5 cm/yr. Displacement measurements and observations inside the gallery showed a succession of rigid moving blocks delimited by highly fractured zones parallel to the main fracture set. These blocks exhibit differential normal faulting movement. Unfortunately, the gallery did not reach sound rock, and the presence of a sliding surface is still an open question.

[12] All these studies suggest that the slope movements at Séchilienne are controlled by the principal discontinuities. The mass breaks into blocks, which are toppling or sliding. The rockslide has evolved from progressive damage to a potential large slide of unknown characteristics. Several investigation campaigns using geotechnical, geophysical, hydrogeological and dating methods were performed on this rockslide (see *Méric et al.* [2005] and *Le Roux et al.* [2009] for reviews). *Guglielmi et al.* [2002] used isotopic and hydrogeochemical methods to investigate groundwater flows. This study showed that the deep groundwater in the low part of the slope is partly recharged from a perched sedimentary aquifer, and that water flows very quickly (several cm/d)

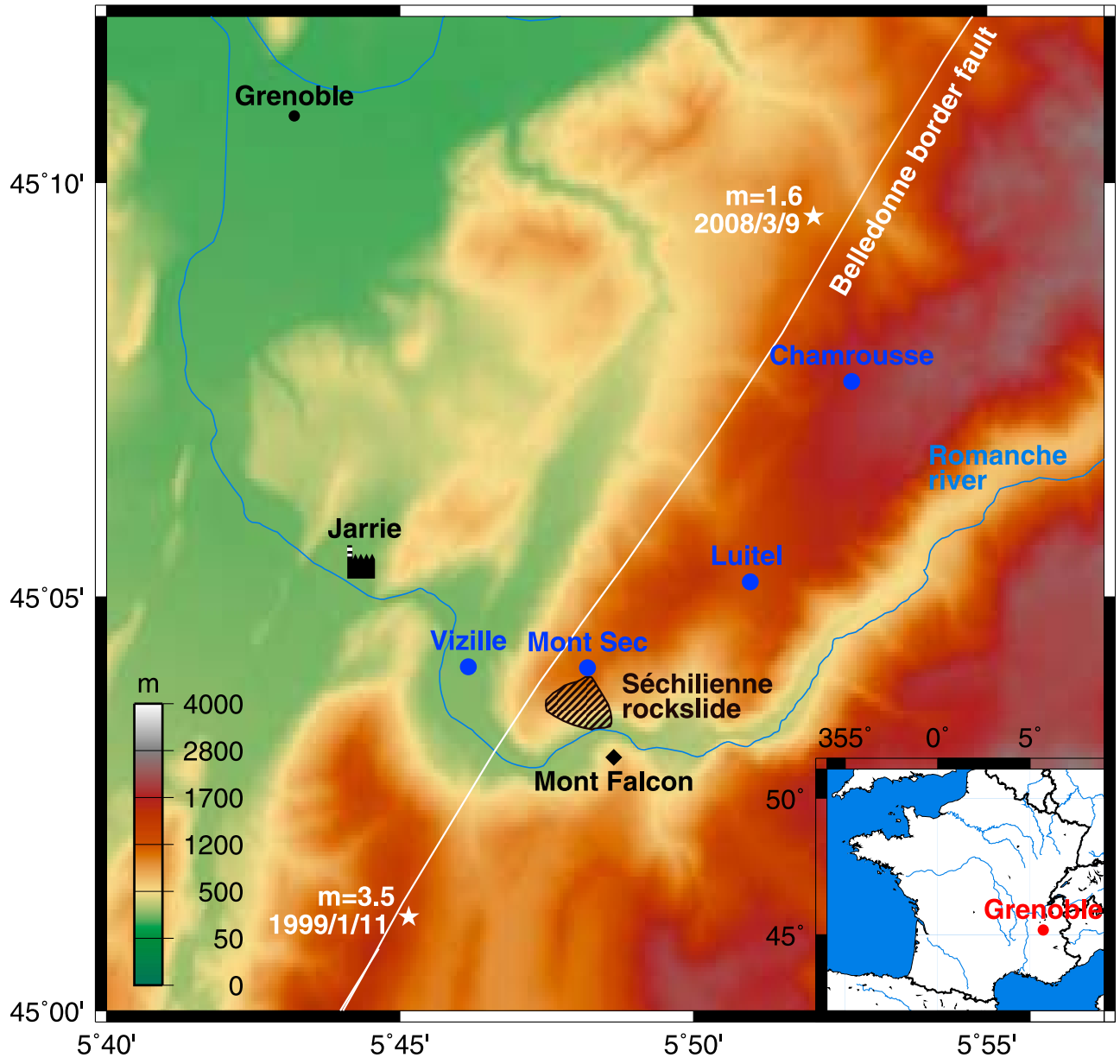

Figure 1. Location of Séchilienne rockslide, in the French Alps, about 15 km southeast of Grenoble, and contour of the rockslide. Also shown are the Belledonne Border Fault (solid line), earthquakes (white stars) and weather stations in the proximity of the rockslide (circles).

through the major fault set (oriented 20°N) affecting the rock mass. This analysis showed the existence of a deep saturated zone extending into the fractured metamorphic bedrock, with a probable 100 m thick vadose zone above. In case of intensive rainfall and prolonged water recharge, this vadose zone could be saturated for a short time, increasing the displacement rate. A major outcome of a multimethod geophysical study performed along various profiles [*Méric et al.*, 2005] is that all zones exhibiting signs of present-time or previous movements (collapse, toppling, sliding) are characterized by high electrical resistivity values ($\geq$3 $k\Omega.m$) and low P wave velocity values (2000 m/s), compared with the undisturbed zones (between a few hundred and 800 $\Omega.m$ for resistivity and more than 3000 m/s for P wave velocity). Combining surface observations and the geophysical results clearly shows that the resistivity increase and the velocity decrease are associated with a high degree of fracturing and with the formation of air-filled voids inside the mass.

[13] Despite all these studies, many questions are still open, particularly those related to the volume and the geometry of the rockslide, the deep hydrological context and the possibility of precursory events such as rockfalls and microseismicity. To address these issues, deep boreholes ($\geq$120 m) have recently been drilled and instrumented with inclinometers, piezometers and seismometers. Piezometers measure fluid pore pressure and water level. Seismometers at depth could help to better constrain the depth of seismic events and consequently to locate more precisely seismogenic zones. In addition, the Séchilienne rockslide is part of a National Observatory in France (denoted "OMIV"), which

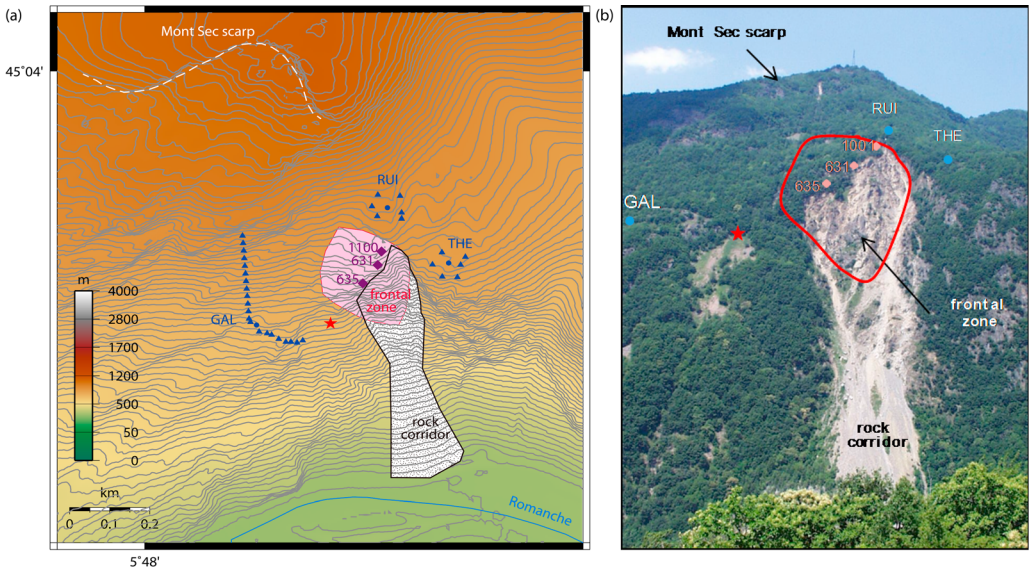

Figure 2. (a) Map of the seismic network: vertical sensors (circles) and 3-component seismometers (triangles) for the 3 stations. (b) Photograph of the rockslide. Also shown are the locations of benchmarks of the displacement network (diamonds) and the location of a shot on 24 June 2008 (red star). The red contour shows the limit of the most active zone. The white dashed line in Figure 2a shows the Mont-Sec scarp.

aims at continuously monitoring several active landslides with different techniques (seismology, geodesy, remote sensing, hydrology).

3. Monitoring Network

3.1. Displacement

[14] A surveillance and alert system based on displacements measurements (laser, radar, extensometers, inclinometers, strainmeters, GPS) was set up and progressively supplemented from 1985 [*Evrard et al.*, 1990; *Effendiantz and Duranthon*, 2002; *Duranthon et al.*, 2003; *Duranthon and Effendiantz*, 2004; *Lemaître et al.*, 2004; *Kasperski*, 2008]. This very dense system has allowed delimitation of zones in movement and their evolution for more than 20 years. It notably has shown that the displacement rate of the most active zone has increased up to 1.4 m/yr in 2008, more than twice the mean rate observed before 2000. The other regions exhibit displacements generally lower than 10 cm/yr. In addition, a camera and video have been installed in June 2009 to detect and characterize large rockfalls, and to estimate displacement from the comparison of successive images.

3.2. Seismic Network

[15] The seismic network was progressively installed from May 2007. It consists of three seismological stations and various receivers, whose locations are shown in Figure 2. Two stations denoted "THE" and "RUI" were first installed in May 2007. Each station was connected to 6 vertical 2 Hz velocity sensors and one 3-component 2 Hz velocimeter. Station RUI is now located just above the most active zone. Before April 2008, it was located 50 m downward, and one sensor was located below the scarp which borders the main active zone. This sensor displayed a very large resonance around 15 Hz, which made it difficult to correlate the signals with the other sensors outside the active zone. To enlarge their frequency sensitivity toward low frequencies, all sensors were replaced in April 2009 by broadband 0.05 Hz NoeMax velocimeters. The typical distance between sensors for these two stations is 50 m. In addition, a 24-channel station, denoted "GAL" (Figure 2), was later installed in April 2008 in the 240 m long survey gallery on the western side of the most active zone. It was connected to 4.5 Hz geophones (21 vertical sensors and one 3 component), with an intertrace of 20 m. Among them, 11 sensors were installed within the gallery and 10 outside the gallery in the eastern direction (Figure 2).

[16] Stations THE and RUI were first recording data in triggering mode, with a STA/LTA threshold fixed to 3, and a 250 Hz sampling frequency. This setting was changed in April 2008 to a continuous mode. Sampling tests conducted over a short period with a higher sampling frequency (1 kHz) showed the near absence of seismic energy above 100 Hz. For station GAL, due to the larger number of channels, the station is working in trigger mode to limit the amount of data recorded. However, a higher sampling rate of 500 Hz is being used, because we thought that small high-frequency microearthquakes may occur close to the end of the 240 m gallery near the base of the rockslide. Until now, however, most events were first detected by the channels located outside the survey gallery and present little energy above 50 Hz.

4. Detection and Classification of Seismic Signals

[17] Since the installation of the first two stations in May 2007, several thousands events have been recorded by each station. A semiautomatic software has been developed to detect and classify events. All events are then visually analyzed to separate natural local events from regional or worldwide earthquakes, and to reject events classified as

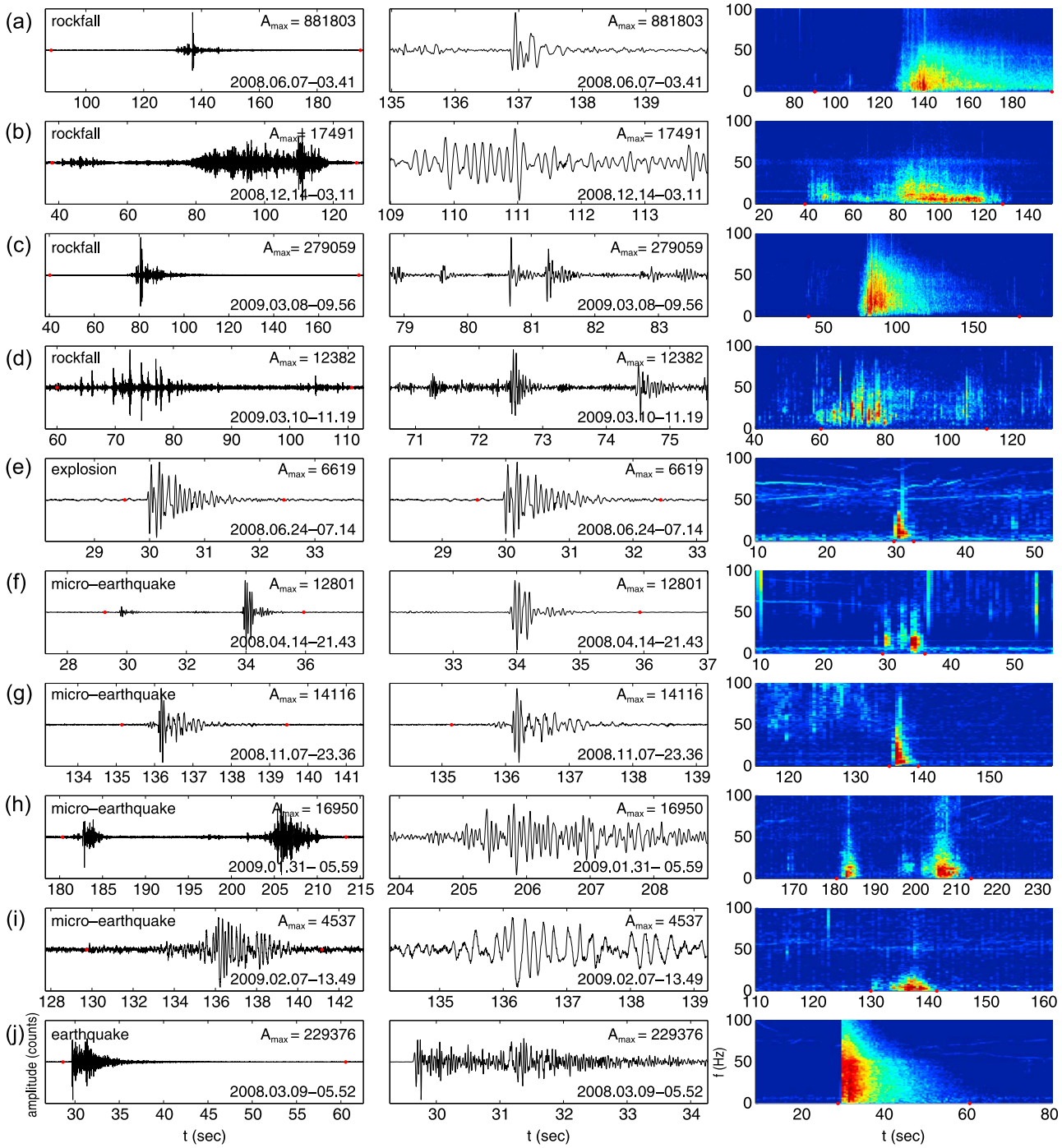

Figure 3. (a–j) A selection of different types of signals. (left) Seismograms recorded for channel 0 of station THE and (middle) zoom for a window of 5 s around the peak of amplitude. The maximum amplitude (in counts) is given in the top right corner of each plot. (right) Spectrograms (log amplitude scale) averaged over all vertical channels of station THE. Dots indicate the start and end of each event.

noise (helicopters, industrial noise, storms). The catalogs of events are available on the OMIV web site: http://www-lgit.obs.ujf-grenoble.fr/observations/omiv/SECHILIENNE.

4.1. Detection of Seismic Signals

[18] The detection of seismic signals is based on the spectrogram of the signal, averaged over all sensors of a seismic antenna (see Figure 3, right). We estimate the amplitude of the spectrogram stacked in the frequency range 1–50 Hz, as a function of time. An event is identified when this function exceeds 3. The event starting time and duration are first defined by the time interval during which the spectrogram amplitude stays above the noise level. This definition leads to a large number of events with very short interevent

times. For instance, a rockfall event may be divided into several events corresponding to successive rock impacts. Consequently, all events with interevent time smaller than their duration are regrouped as a single event.

4.2. Location of Seismic Signals

[19] Event location is difficult because most recorded signals lack impulsive waves so that a satisfying time picking of first arrivals is almost impossible (see Figure 3), even for large amplitude signals. Instead, one can use cross correlation of signals recorded at different sensors in order to precisely measure time delays between sensors, or beamforming methods [*Almendros et al.*, 1999]. The latter amounts to looking for the source point which maximizes the intertrace correlation, averaging over all couples of sensors and after shifting traces in time by the travel time. A second difficulty concerns distinguishing P from S waves, because of the small distances between the source and the sensors and of the lack of high-frequency waves. For distances of a few hundred meters, the time delay between P and S waves is a few hundredths of a second, of the order or even shorter than the dominant period of the signal (generally between 10 and 20 Hz), so that P and S waves overlap. In the absence of a precise 3-D velocity model, a uniform velocity was used. The source depth was constrained to lie at the ground surface and velocity was inverted in the interval 1000–4000 m/s.

[20] Clearly, a uniform velocity model is not realistic in such an heterogeneous rockslide, and in many cases this simple model was not able to correctly explain the observed time delays between sensors. Indeed, 2-D seismic tomography studies realized by *Méric et al.* [2005] have shown a very complex structure. P wave velocity varies laterally and with depth, ranging from about 500 m/s to almost 4000 m/s in undisturbed areas. A correct 3-D velocity model is thus required in the future to better locate seismic signals. This represents a challenging task in such an heterogeneous and mountainous area and will be obtained from supplemental active seismic profiles, which must be performed on a larger scale in order to build a deeper 3-D velocity model. In this work, we do not present the preliminary results on event location. Nevertheless, event location was routinely estimated and used to better discriminate seismic signals. For instance, distant earthquakes can be recognized by their high apparent velocity due to their large dip angle. Rockfalls can be identified by their azimuth evolving during their propagation, which is consistent with a source moving downward along the rock debris corridor [*Helmstetter et al.*, 2008]. Events which could not be successfully located (averaged intertrace correlation less than 0.5) were rejected as probable noise events.

4.3. Different Types of Signals

[21] Figure 3 presents a selection of ten signals of different types. Data have not yet been deconvolved by the instrument response so signal amplitude is given in counts (see peak amplitude in the caption of each plot). For each signal, we show the seismogram for the whole event duration and for a window of 5 s around the peak amplitude, and the associated spectrogram. The first four examples are rockfalls. Events from Figures 3f–3i are local microearthquakes. Seismic signals displayed in Figure 3e originated from an explosion performed using a charge of 1 kg located at 1 m depth, 350 m away from the sensor across the most active zone (Figure 2). The charge used corresponds to a magnitude of about 0.3 [*Brocher*, 2003]. The peak amplitude for this shot was A = 6620 counts, about half the amplitude of the largest recorded microearthquake, shown in Figure 3g with A = 14100. Because this event was likely located in the most active zone, closer to the sensor but with an amplitude twice as large, its magnitude should be close to the one deduced from the shot, around 0.3. The last signal is an earthquake of magnitude m_l = 1.6, detected by Sismalp seismological network and located about 12 km north of the rockslide. None of the local signals recorded at Séchilienne has been detected by Sismalp, although the closest station is about 20 km away. Even the 23 November 2006 rockfall, with a volume of about 40,000 m^3 [*Kasperski*, 2008], was not detected by Sismalp.

4.3.1. Rockfalls

[22] Most natural local seismic events which were recorded correspond to rockfalls, which are frequent at Séchilienne, especially in the rock corridor located around the frontal zone. A 40,000 m^3 rock avalanche occurred in this area in November 2006 [*Kasperski*, 2008]. Since the installation of the seismic network, only a rockfall of about 250 m^3 has been observed by people in charge of the surveillance and though reported as having occurred in July 2008, the exact date of this event is unknown. It may correspond to one of the largest events, recorded on 14 July with a peak amplitude of A = 165,000. Other rockfalls of this size may have occurred without having been reported, particularly if they occurred in zones with dense vegetation or if they presented less spread. The largest rockfall recorded occurred on 7 June 2008, with an amplitude A = 882,000 (see Figure 3a), but there was no reported observation of rockfall around this date. Seismic signals present generally a broad spectrum, sometimes spanning the full 1–125 Hz available range. Smaller events exhibit the highest energy around 20 Hz, while larger events present a peak below 10 Hz. Some events, such as the one in Figure 3b, have little energy above 20 Hz. The low-frequency spectral content of these events may be due to the larger distance from the stations, because they are located further down the debris corridor and high-frequency waves are attenuated faster, particularly in such a fractured and heterogeneous medium. Low-frequency events are generally located south of station THE, while the large-band signals are generally located west or southwest from this station, likely within the upper part of the debris corridor. The differences in frequency content may also be explained by differences in entrained materials, i.e., debris flows instead of rockfalls, or by different propagation conditions. Indeed, in the upper part of the corridor, rocks often hit the ground and rebound, producing distinct impulsive peaks in the seismograms, while in the lower part of the corridor rocks tend to roll and to trigger other small rockfalls, or burst into smaller rocks.

[23] In general, event durations are of the order of several tens of seconds. Some events are shorter either because rocks do not fall all the way down the corridor or because later impacts are too weak to be detected. The longest events lasted for several minutes, because several avalanches overlap, or because rocks fall continuously from the upper slopes. The smallest events are difficult to distinguish from microearthquakes because there is only one or a few peaks.

By default, local natural events were classified as rockfalls, so the classification is often inaccurate for low-amplitude signals.

[24] With the intention of calibrating our network for small events, a small rock of dimensions about 0.5 × 0.5 × 0.2 (small volume of 0.05 m^3 selected for security reasons) was thrown from the upper part of the rock corridor in order to compare the recorded signal with natural events. The corresponding seismogram is shown in Figure 3d. In terms of amplitudes, the peak was 12,000, much smaller than the largest recorded rockfall. The corresponding seismogram shows several distinct events associated with successive rock impacts. The rock fell for about 30 s over a distance of about 400 m. The following peaks in the seismograms (after 100 s) are due to other small rocks falling down another part of the rock corridor. Compared with the natural events shown in Figures 3a–3c, this event does not show a long-period prolonged ringing. This could be because it involved only one block, while large natural events likely involve many blocks. However, we also observed natural events which displayed characteristics similar to those of the experimental rockfall.

[25] Assuming rockfall volume is proportional to peak amplitude, as suggested by *Norris* [1994], the largest recorded rockfall would have a volume around 4 m^3. This volume appears very small because much larger events are known to have occurred since the network installation. This volume may be underestimated if either natural events occurred farther away from the seismometer or if rockfall volume increases more rapidly than seismic peak amplitude. The video camera, installed in June 2009 and facing the landslide, should enable us to calibrate the seismic network. It will allow us to estimate the nature of the materials involved (rockfalls or debris flow) and to study the relation between the involved volume and the recorded signal amplitude and frequency content. This requires events large enough to be observed with the video camera, occurring during a day without clouds.

4.3.2. Local Microearthquakes

[26] Microearthquakes can be distinguished from rockfalls by their shorter duration, typically a few seconds. Examples are shown in Figures 3f–3i. They have about the same frequency content, although the largest events exhibit generally more energy at low frequencies (below 10 Hz) than rockfalls. There is also a large variability of signal waveform, duration and frequency content. Some events, such as the one shown in Figure 3g, exhibits waveform characteristics rather similar to the shot shown in Figure 3e in terms of duration, frequency content and amplitude. The largest arrival of this quake is preceded by an emergent signal, starting about 0.2 s before, of much weaker amplitude. Other events consist of several subevents, separated by about 1 s or longer. Examples are shown in Figures 3f and 3h.

[27] Compared to distant earthquakes (see the largest one recorded in Figure 3j), microearthquakes lack high-frequency waves. This low-frequency content may be due to the source of these events or to the strong attenuation of high-frequency waves within the fractured zone. These events may be associated with water flow within the fractures, similar to long-period earthquakes induced by magma flow on volcanoes. Another possibility is that this unusually low frequency content results from low rupture velocities combined with strong path effects due to their shallow sources, as first suggested by *Harrington and Brodsky* [2007] for volcanic earthquakes. Other microearthquakes exhibit a broadband spectrum, comparable with distant earthquakes. They occur either individually or as a sequence of a few events, with interevent times of about 1 s (see Figure 3g). Microearthquakes can be distinguished from distant earthquakes by their absence of distinct P and S waves and by their lower apparent velocities, because of their shallower depth. Most local events (microearthquakes or rockfalls) have an apparent velocity of about 2 km/s, while for earthquakes $V > 4$ km/s due to their higher dip angles.

4.3.3. Distant Earthquakes

[28] Many earthquakes have been recorded, 773 in less than 2 years. About half of these events have also been detected by the Sismalp regional network. Most of the missing events are nearby earthquakes, with interevent times between P and S waves in the range of 0.5–2 s, corresponding to a distance of about 4–16 km. Their magnitudes are likely smaller than 1, which is the detection threshold of Sismalp network in this area. As mentioned before, the Séchilienne rockslide is located within an active seismogenic zone close to the Belledonne Border fault [*Thouvenot et al.*, 2003]. So far, the largest signal recorded by our network is the 2008/3/9 $m_l = 1.6$ earthquake, located about 12 km to the northwest. It is displayed in Figure 3j. Before the installation of the seismic network, a $m_l = 3.5$ earthquake occurred about 7 km southwest of Séchilienne, on the southwestern ending of the Belledonne fault, followed by a $m_l = 2.8$ event in October 2005 [*Thouvenot et al.*, 2003]. The mean recurrence time of a $m \geq 6$ earthquake on this fault has been estimated to be about 10,000 years. As it could occur only 1 km away from the landslide, any risk assessment study should account for possible triggering of the rockslide by an earthquake.

4.4. Distribution of Signal Amplitude, Duration, and Energy

[29] Figure 4a presents the distribution of signal amplitudes for rockfalls (type R) and microearthquakes (type Q). The amplitude was estimated after low-pass filtering seismograms below 50 Hz, and after averaging maximum amplitude of all 7 vertical channels of station THE. The distribution follows a power law for amplitudes larger than 1000. For smaller events, the curvature is likely due to the incompleteness of the catalog because of temporal fluctuations of the noise level. The slope exponent is 1.1 for rockfalls and 1.6 for quakes. These exponents can be compared to the b value of the Gutenberg-Richter distribution of earthquake magnitudes, $b \approx 1$, if we assume that most events are located at about the same distance from the station so that amplitude variations according to distance from the source are limited and do not modify the shape of the distribution [*Weiss*, 1997].

[30] Figure 4b shows the distribution of energy, defined as the envelope of the signal integrated over event duration. For quakes, the distribution can be fitted by a power law of exponent 1.2, while for rockfalls, the distribution is curved in a log-log plot over the whole interval, and cannot be fitted by a power law.

[31] The distribution of signal durations is shown in Figure 4c. It can be fitted by a power law over a limited

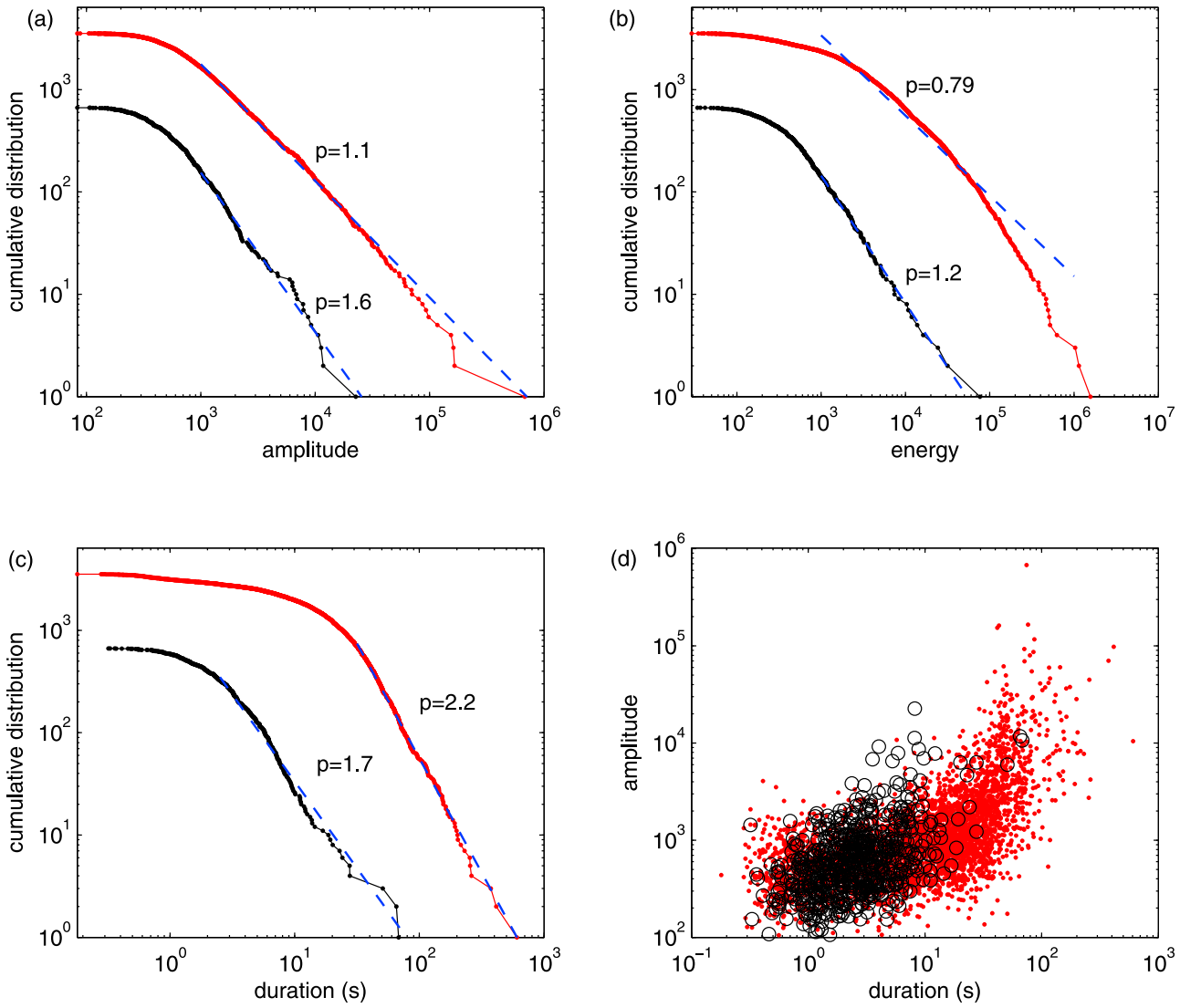

Figure 4. (a) Distribution of the peak amplitude A of rockfalls (red curve) and microearthquakes (black) and fit by a power law for $A > 1000$ (slope exponent is given in the plot), (b) distribution of signal energy (signal envelope integrated in time) for rockfalls (red curve) and microearthquakes (black) and fit by a power law for $E > 1000$ (see slope exponent in the plot), (c) distribution of event duration for rockfalls (red curve) and microearthquakes (black) and fit by a power law, and (d) relation between peak amplitude and signal duration for rockfalls (red dots) and microearthquakes (black circles).

interval; for microearthquakes longer than 2 s and for rockfalls with duration larger than 30 s. For rockfalls, this duration of 30 s corresponds to the time taken for a rock to fall from the upper part of the corridor down to the valley. Longer events are sequences of rockfall avalanches with interevent times smaller than their duration (which were therefore counted as a single event). Microearthquakes with duration longer than 5 s are generally sequences of shorter subevents. The relation between peak amplitude and duration for quakes and rockfalls is shown in Figure 4d. Rockfall duration may be underestimated for small rockfalls, because only the more energetic impacts are above the detection threshold. Also, as distinguishing quakes from rockfalls is difficult for small events, they were classified as rockfalls by default. The amplitude-duration relation is rather similar for quakes and rockfalls, but the largest quakes exhibit a shorter duration than rockfalls with the same peak amplitude.

5. Influence of Rainfall on the Rockslide Dynamics

5.1. Meteorological Data

[32] At least 5 meteorological stations or rain gauges are located within 10 km of the rockslide (Figure 1). The closest station (maintained by CETE Lyon) is located at Mont-Sec, but presents several gaps in the data, and has a large sampling time of 1 day, leading us to preferentially use other rain gauges. The Luitel rain gauge is located 4 km northeast from the landslide at a higher elevation (1280 m). It is maintained by the "Laboratoire d'étude des Transferts en Hydrologie

et Environnement," and data are available since July 2007. This is our preferred station because it has a fast sampling time of 15 min with few gaps in the data. Another gauge is located at Vizille, about 3 km west from the rockslide at an elevation of 290 m. It has a sampling time of 5 min and was placed in operation in September 2007 (http://pagesperso-orange.fr/meteo.vizille). The last station is located at Chamrousse, about 10 km to the northeast of the rockslide at an elevation of 1860 m. It is part of Meteo France network and has been working with few gaps since the installation of our network, with a sampling rate of 1 h. It was used to fill in the gaps observed at other stations. We tested every meteorological station to analyze the influence of station location on the correlation between landslide dynamics and precipitation. Only weak differences were found.

5.2. Temporal Evolution of Microseismicity, Rockfall Activity, Rockslide Movement, and Weather

[33] Figure 5 illustrates the temporal variability of the rockslide dynamics since the installation of the seismic network in May 2007. All events detected by station THE are shown in Figure 5a, but only events with amplitude larger than 500 were used to estimate the daily rate displayed in Figure 5b. Quakes and rockfalls occur in bursts of activity, lasting for a few days, and appear very often correlated with rainfall (Figure 5d) and acceleration of the rockslide displacement (Figure 5c). Quakes generally occur during episodes of rockfalls, but rockfalls were relatively more frequent in June 2007 and June 2008, and quakes occurred more frequently and continuously in the winter 2008 (see cumulative number of events in Figure 5b). This may be due to continuous snowmelt inducing continuous water flow within the rockslide.

[34] Rockslide movement also fluctuates with time. Figure 5c shows the displacement rate of benchmark 635, located in the most active zone (Figure 2). This is one of the most rapidly moving targets that presents no gaps during the time period considered, except after March 2009, because data are not yet available. Daily displacement rate increases almost instantaneously following rainfall [*Alfonsi*, 1997; *Duranthon and Effendiantz*, 2004], and decreases back to its mean value within about 2 months. The temporal evolution of displacement rate has been successfully modeled by *Alfonsi* [1997], assuming that velocity increases with the amount of water (rainfall or snow, decreased by evapotranspiration) received by the rockslide, and that the groundwater table decreases exponentially with time in the absence of precipitation. However, seasonal variations of the hydrological parameters are required in order to correctly model the observations.

5.3. Thresholds for Rainfall Triggering?

[35] Correlation between rainfall and rockfalls is not striking when looking at the temporal evolution of rainfall and daily rates of rockfall in Figure 5. Using traditional diagrams showing rainfall intensity versus duration, introduced by *Caine* [1980], is not very helpful. *Caine* [1980] first plotted each landslide occurrence in a diagram showing the precipitation at the time of each event as a function of the rainfall duration, for a catalog of worldwide shallow landslides and debris flows. He observed that all events occurred above a threshold I_r (in mm/h) defined by $I_r = 14.82\ D^{-0.39}$, where D is the storm duration in hours. Such a plot is shown in Figure 6 (circles) for all rockfalls recorded with amplitude greater than 500. A rainfall episode is considered finished as soon as there is a gap of 1 day without rain. It is impossible to define a minimum threshold for triggering from Figure 6. Most events occur for zero or very small rainfall intensities, and consequently no apparent relation can be derived between the density of events and the rainfall intensity or duration.

[36] Other types of thresholds have been proposed using the rain accumulated from the beginning of the rainfall until the landslide occurs, or the total rainfall stacked over a period of a few days up to a year before the landslide occurs, or more complex physically based thresholds (see *Guzzetti et al.* [2007] for a recent review). Similar results were found when replacing the hourly rainfall by the cumulated rainfall before the event. A problem arising with these thresholds is that, when new data are added to the database, landslides may be observed for rainfall conditions lower than the minimum threshold, so that a new threshold has to be defined [*Chleborad et al.*, 2006]. Thresholds describe the minimum rainfall above which landslides may occur. A maximum threshold is sometimes introduced to give the maximum rainfall above which landslides always occur. But this approach does not tell us how likely landslides are between the minimum and maximum thresholds. Also, only landslides triggered by rain are considered in these studies, giving up those which were triggered by earthquakes or by an unknown mechanism.

[37] Few studies have attempted to quantify the probability of landslide occurrence as a function of rainfall properties (either rainfall duration, intensity, or cumulated rainfall, or a combination of these parameters). *Glade et al.* [2000] have estimated this probability as a function of daily rain at the time of the landslide and as a function of the "antecedent daily rainfall index." *Guzzetti et al.* [2007] also estimated the probability of landslide occurrence as a function of rainfall duration and intensity. In section 5.4, we use a model inspired by the "Antecedent Daily Rainfall" model of *Glade et al.* [2000] in order to quantify the probability of rainfall triggering at Séchilienne.

5.4. Antecedent Rainfall Water Model

[38] We have modeled the observed temporal variations of rockfall activity using a method inspired by the Antecedent Daily Rainfall model [*Crozier and Eyles*, 1980; *Glade et al.*, 2000]. We define the cumulated rainfall index P_c at time t_i by

$$P_c(t_i) = \sum_{j=0:i} P(t_j) \exp\left(-(t_i - t_j)/t_c\right). \quad (1)$$

P_c is the sum of hourly rainfall, and rainfall of all previous hours with a weight exponentially decreasing with time. This model accounts for the decay of the amount of water with time due to drainage. The rate of rockfall activity $R(t)$ is then assumed to vary linearly with $P_c(t)$. Only events with $A > 500$ were used together with rainfall data measured at Luitel meteorological station, with a sampling rate of 1 h.

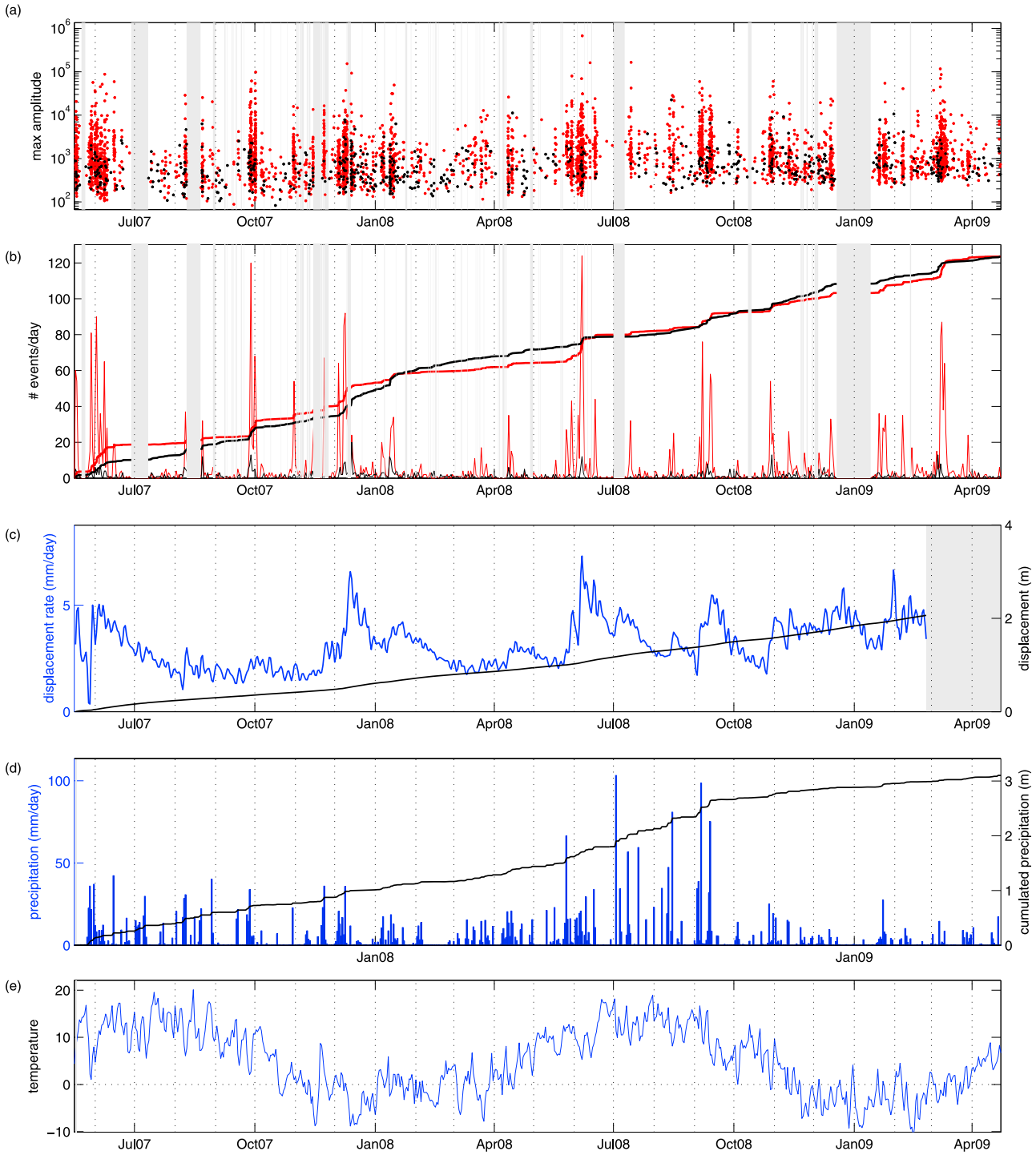

Figure 5. (a) Time series of event peak amplitude for rockfalls (red dots) and microearthquakes (black dots). Gray areas indicate gaps in the monitoring. (b) Daily rates of rockfalls (red) and microearthquakes (black) and normalized cumulated number (smooth red and black lines). (c) Displacement rate (blue line) and displacement (black) of benchmark 635 (data are not yet available after March 2009). (d) Daily and cumulated rainfall and (e) daily average temperature recorded at Luitel meteorological station.

We estimate the characteristic time t_c = 0.25 day by maximizing the linear correlation coefficient between $R(t)$ and $P_c(t)$.

[39] Figure 7 compares the time series of rainfall, cumulated rainfall, and number of rockfalls per hour, for a time window of one month in September 2008. Peaks of rockfall activity are rather well correlated with cumulated rainfall, although some events have occurred in the absence of rainfall. Figure 8 shows the correlation between the number of events per hour and rainfall. When looking at the raw rainfall

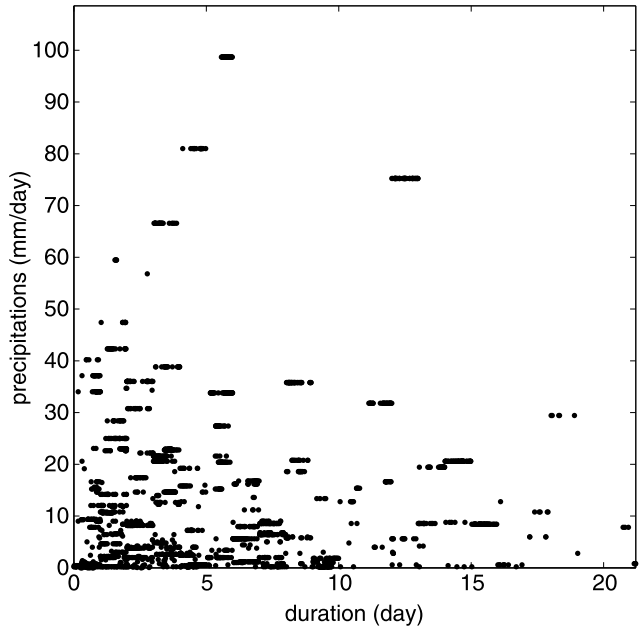

Figure 6. Rockfall occurrence (events with $A > 500$) as a function of the duration of the rainfall episode until each event and of the daily rainfall at the time of the event.

data as a function of number of rockfalls (hourly rainfall or $P_c(t)$, shown as crosses in Figures 8a and 8b), the correlation is not obvious. There are indeed large fluctuations of the number of rockfalls for the same rainfall value. But when averaging the number of rockfalls for different classes of rainfall (using a sampling bin size of 1 mm), we now better observe an increase in rockfall activity with precipitation (dots in Figures 8a and 8b), which becomes stronger when looking at cumulated rainfall rather than hourly rainfall.

[40] Using all hourly values of rate and rainfall (crosses in Figures 8a and 8b), the correlation between $R(t)$ and $P_c(t)$ is 0.36, a little larger than the correlation with hourly precipitation, equals 0.25. Taking into account antecedent rainfall in the model thus improves the correlation between rockfall activity and rainfall. In both cases this correlation is highly significant, the probability of getting the same correlation by chance being almost zero. However, if we fit the data after averaging in classes of rainfall values (i.e., fitting the red curve with dots in Figures 8a and 8b), the correlation is then only significant for cumulated rainfall. This approach gives the same weight to any rainfall interval, while fitting the raw data of $R(t)$ and $P_c(t)$ gives the same weight to each time interval, so mostly to small rainfall values. After increasing for rainfall smaller than 10 mm/h, the number of events per hour appears to stabilize or even decrease. We think that this is mostly due to the limited number of observations for large rainfalls. Rockfall rate increases from 0.14 per hour up to about 2.5 events per hour when rainfall increases from 0 to 10 mm/h. Figure 8c shows the cumulated distribution of rainfall at the time of a rockfall event. About 49% of events have occurred when the hourly rainfall was zero, and 94% when rainfall was less than 5 mm/h. Only 2% have occurred when rainfall was larger than 10 mm/h.

5.5. Cross Correlation of Microseismicity, Rockfall Activity, and Weather

[41] In order to study the correlation between rainfall and rockfalls at Séchilienne, we have used the cross-correlation function between the rate of rockfalls R and the precipitation P, defined by $C_{R,P}(t) = \sum_i R(t_i)P(t_i + t)$. The variables R and P were first detrended (removing average value) and normalized by their standard deviation, so that $C_{R,P}(0)$ (for zero time lag t) denotes the linear correlation coefficient of P and R (equals 1 for perfect correlation, −1 for anti-correlation). The cross correlation of R and P can be interpreted as the average precipitation as a function of time before and after a rockfall occurrence. This method allows comparison between rockfall occurrence and previous rainfall. It is useful to quantify the correlation and to estimate the time delay between precipitation and triggered rockfalls. Figure 9a shows the cross correlation between hourly precipitation recorded at Luitel and the number of rockfalls per

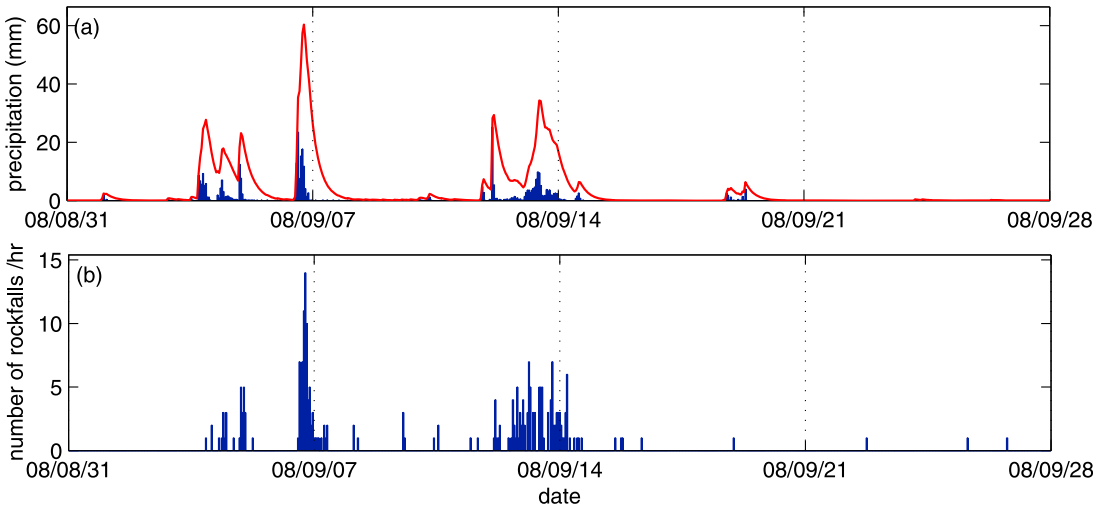

Figure 7. (a) Hourly rainfall (blue bars) and cumulated rainfall (red curve) and (b) hourly number of $A > 500$ rockfalls in September 2008.

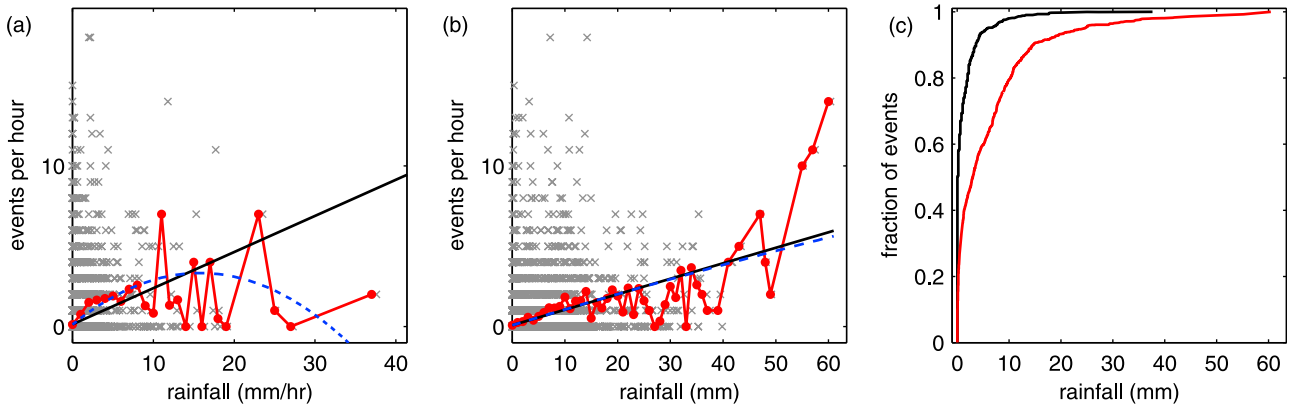

Figure 8. Number of rockfalls per hour with $A > 500$, as a function of (a) hourly precipitation and (b) cumulated precipitation (crosses). The solid line is a linear fit of all hourly values, and the dashed line is a fit by a second-order polynomial. Dots represent the average value of rockfall rate, obtained by binning the rainfall data with a bin width of 1 mm. (c) Fraction of events that have occurred for precipitation smaller than a given value as a function of this threshold. Black line is for hourly precipitation, and red line is using cumulated precipitation.

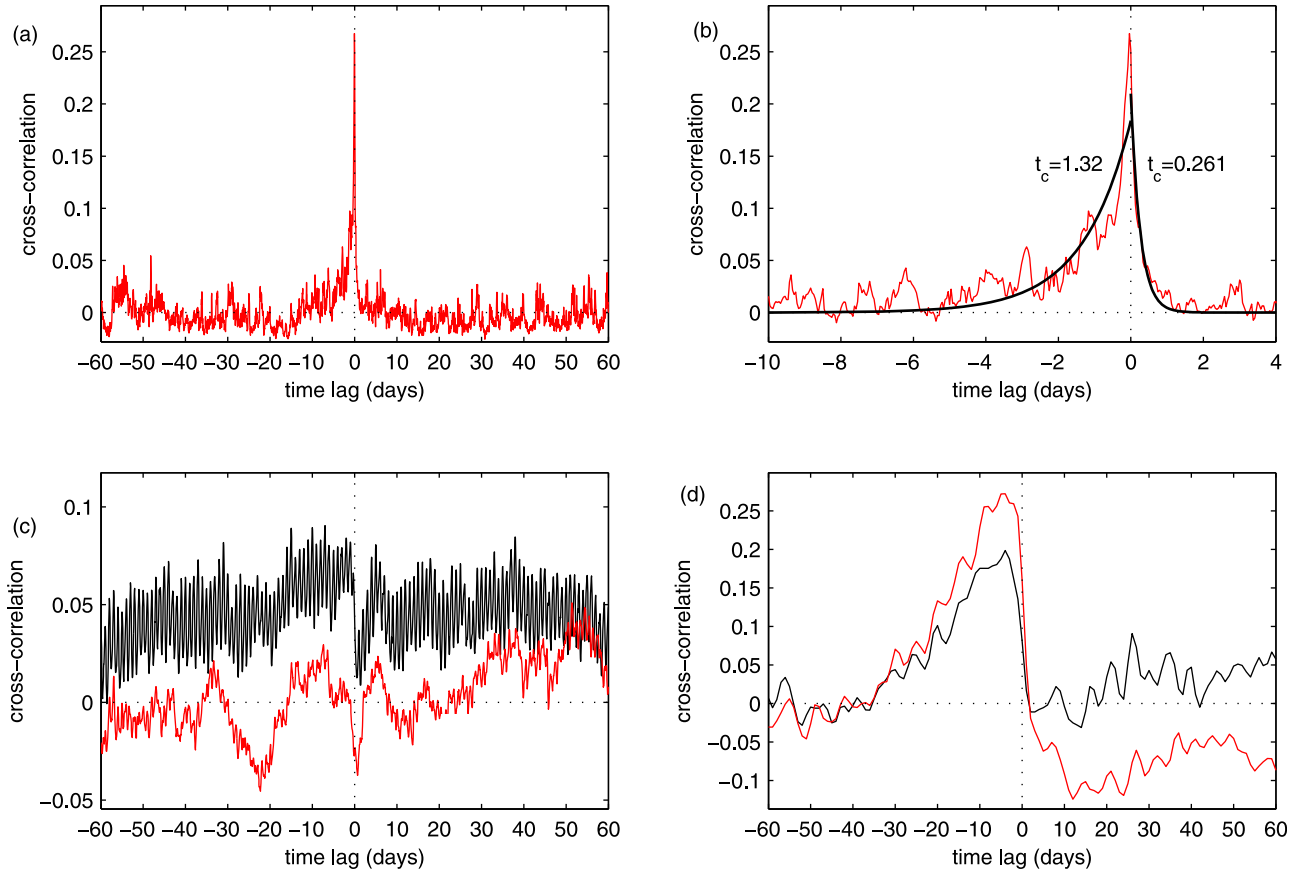

Figure 9. (a) Cross-correlation function of hourly rate of rockfalls and hourly precipitation recorded at Luitel rain gauge; (b) zoom for short time delays, and fit by an exponential law $\sim\exp(-|t|/t_c)$, for both negative and positive times; (c) cross-correlation function of hourly rate of rockfalls and temperature (red line) and of temperature and rainfall (black); and (d) cross correlation of daily precipitation and displacement rate of benchmark 635 (black curve) compared with the cross correlation of displacement rate and daily rate of rockfalls (red line).

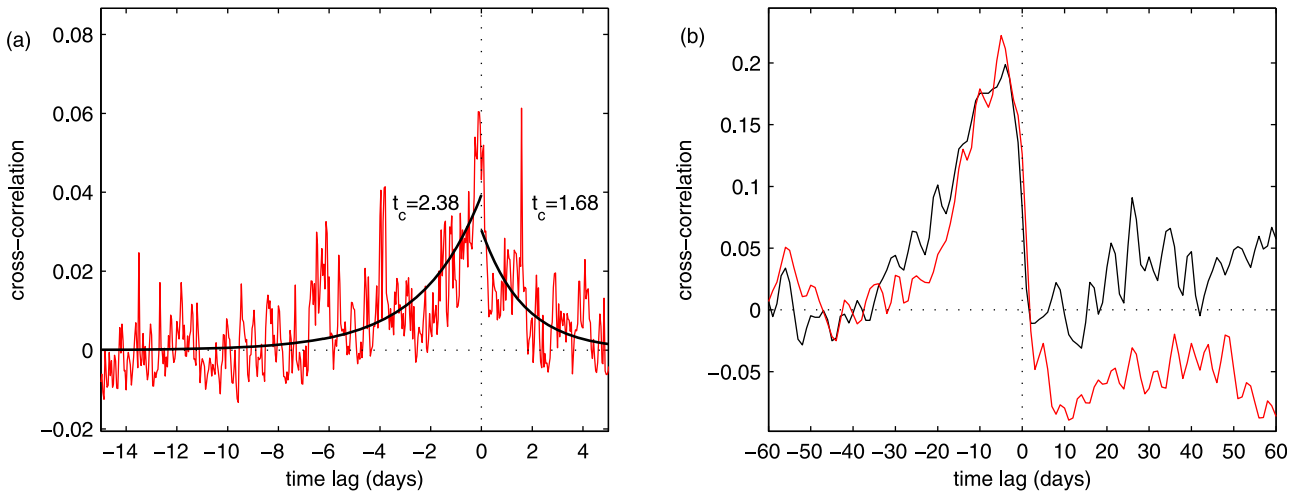

Figure 10. Same as in Figures 9b and 9d for microearthquakes.

hour. We used 3098 rockfalls recorded by station THE with peak amplitude above 500. In order to minimize the influence of gaps in the seismic monitoring, the precipitation was set to zero during gaps before computing $C_{R,P}(t)$. The cross correlation displays a maximum value of 0.27 for a time delay of 1 h (sampling rate) between precipitation and rockfall activity. The peak amplitude is much larger than the average value, indicating that the correlation is weak but significant. A zoom for shorter time delays is shown in Figure 9b. The peak of the cross-correlation function is asymmetric. It is wider for negative times (rain precedes seismicity) than for positive times. This shows that rockfalls are not only sensitive to hourly rain, but also to previous rainfall, due to water infiltration or snowmelt. Rockfalls may also trigger future events, thus increasing the duration of rockfall crisis after the end of the rainfall episode. The correlation function for short time delays can be fitted by an exponential law $C(t) \sim \exp(-|t|/t_c)$, with a correlation time t_c = 1.3 days for negative times, and 0.26 days for positive times. The fit is however not perfect as the curvature of the data is stronger than the fit. But in a log-log plot, $C_{R,P}(t)$ exhibits a convex shape, so that it cannot be fitted by a power law over a significantly large time interval. The variation of $C_{R,P}$ with time is thus intermediate between an exponential and a power law function.

[42] To access shorter times delays, we used Vizille rain gauge, with a sampling time of 5 min. We found that the peak of $C_{R,P}(t)$ occurs at $t = -25$ minutes. Using Luitel rainfall data, sampled at 15 min, the correlation peaks for $t = -45$ minutes. It is not clear at present if there is a finite time delay for triggering rockfall, due for instance to the time necessary for water infiltration, or if this delay is due to the distance between the rain gauges and the rockslide. Using rain gauge data sampled every 5 min at Vizille, the peak value is only 0.12, much smaller than when using Luitel hourly data, but this effect is due to the higher sampling rate. Using hourly data recorded at Vizille, the maximum correlation is 0.29, close to the value obtained with Luitel rain gauge. Peak correlation further increases up to 0.47 when using daily rain recorded at Luitel. The same approach was used to study microearthquakes (Figure 10a), using 376 events with $A > 500$. The shape of the cross-correlation function between rate of quakes and precipitations is similar to the results obtained for rockfalls, but the correlation is weaker, and has a peak for $t = -3$ h. Using hourly data, the peak is 0.06, compared to 0.27 with rockfalls, but it is still above the noise level.

[43] There is also a weak but significant negative correlation between temperature and rockfall activity (Figure 9c). Maximum of activity coincides with a decrease of temperature. While a decrease of temperature below 0°C is known as a potential mechanism for rockfall triggering [e.g., *Frayssines and Hantz*, 2006], we do not think that freeze-thaw cycles can explain the correlation between rockfalls and decreasing temperature at Séchilienne. The largest peaks of rockfall activity have been observed in October 2007 and June 2008, when temperatures always remained positive. We rather suggest that this correlation results from the correlation between temperature and rainfall (red curve in Figure 9c), because precipitation is usually associated with a temperature drop. Indeed, the cross correlation between rainfall and temperature is very similar to $C_{R,P}(t)$, for both the shape and the peak value.

5.6. Cross Correlation of Rockfalls, Microearthquakes, and Displacement

[44] Both rockfalls and microearthquakes were found to be significantly correlated with accelerations of the rockslide displacement (Figures 9d and 10b). For rockfalls, the peak occurs for $t = -4$ days; that is, peak of rockfall activity precedes peak of landslide velocity by about 4 days. The cross correlation is very asymmetric, as it is above zero for $-36 < t < 2$ days. Peak velocities are thus delayed by a few days relative to a crisis of rockfall activity, and velocity relaxes more slowly. This correlation probably mainly results from the correlation of rockfalls with rain, and of rain with displacement. The cross correlation of precipitations and displacement, shown in Figure 9d, is also positive in the time interval $-36 < t < 2$ days, with a peak at $t = -4$ days. The maximum value of 0.2 is however smaller than the peak of cross correlation between rockfalls and displacement rate, equal to 0.26. We have used the data for benchmark 635 in

Figures 9d and 10b, because it has no gap since the installation of the seismic network. Benchmarks 1011 and 631 are also located within the most active zone, and move slightly faster than benchmark 635 (see Figure 1). However, benchmark 631 was destroyed in July 2008 after a rock collapse, and no data are available for benchmark 1011 in January 2009. These two benchmarks produce a higher correlation with precipitation and rockfall activity. Data are also available for other benchmarks located outside the frontal zone, but the correlation with rockfalls and rainfall is very weak. The result that correlation increases with average landslide velocity probably only results from the higher signal-to-noise ratio available in hourly displacement data. This suggests that precipitation is not the only forcing controlling rockslide dynamics. For microearthquakes, the time of the peak is −5 days, slightly larger than for rockfalls, but the correlation decreases faster to zero (Figure 10b). Also, the peak value is slightly smaller, about equal to the maximum cross correlation between precipitation and displacement rate.

6. Discussion and Conclusions

[45] The seismic network installed in 2007 at the Séchilienne landslide has now recorded several thousands events, mostly rockfalls, and also hundreds of local microearthquakes and regional earthquakes. Local microearthquakes generally exhibit less high-frequency energy than distant earthquakes, but the frequency content appears very variable among those events. The lack of high-frequency waves may be due to the strong attenuation of seismic waves in the damaged zone, as shown by recorded signals generated by active shots in this area. Another explanation can also originate from the source, which may generate few high-frequency waves if they are induced by fluid flows, or because of low rupture velocities or strong path effects. The source of these signals is not well understood, in part because their location is presently inaccurate. A deeper and more dense active seismic tomography study is in progress, which will permit derivation of a realistic 3-D P wave seismic velocity model and better location of a few hundred events recorded by all 3 stations. This will help us to understand the nature of the signals recorded, and will also illuminate the most active fractured zones of the rockslide and assess the potential presence (or absence) of a sliding surface. Rockfall volumes are currently unknown, the largest event having likely a volume of about 100 to 1000 m^3, and the smallest ones being much smaller than 0.05 m^3. Seismic monitoring is thus a very sensitive method for monitoring rockfall activity as it provides a continuous monitoring, with accurate event times and durations. In the near future, we hope to estimate rockfall volume, location, and propagation velocity from seismic signals. A video camera will be a good complement to better understand the nature of the material involved (rock avalanches or debris flows) and calibrate their volumes. However, video will only work during daylight and will be inefficient if the weather is too cloudy, which is frequent during episodes of rockfall activity, or because of dust clouds during rockfalls.

[46] Rockfall activity and microseismicity were found to be weakly, but significantly, correlated with rainfall. No threshold was found for rainfall triggering: even 1 mm of rain is enough to trigger rockfalls, and most rockfalls occur spontaneously in the absence of any precipitation or any other forcing. The probability of rockfall occurrence was found to linearly increase with rainfall (either daily rainfall or antecedent rainfall). Taking into account antecedent rainfall clearly improves the correlation between rockfall occurrence and rainfall. From the cross correlation of rainfall and rockfall, we suggest that rockfall activity starts immediately during a rain episode and lasts for a few days after the end of the rainfall. This time delay can be explained by water infiltration or snowmelt, or by a nucleation process (time taken for motion to displace portions of the toe enough to affect toe stability, or time delay in the conversion of aseismic toppling to seismic rockfall). The relaxation of rockfall activity following rainfall may also be due to the triggering of rockfalls by previous events.

[47] Although rockfall occurrence increases with rainfall, only a small proportion of rockfall events have occurred during the largest rain episodes. Indeed, only 2% of events have occurred when precipitation was larger than 1 cm/h. Thus the probability of a moderate rockfall being triggered by a large rainfall is very small because the probability of rockfall occurrence increases more slowly with the rainfall intensity than the decrease of the rainfall distribution.

[48] If these observations, based on moderate rainfall and small rockfall volume, can be extrapolated to much bigger events and intense precipitation, then these results could have implications for estimating the coupled hazard of a flood resulting from a slope failure. Hazard assessment studies generally assume that slope failure will occur during an exceptional rainfall, thus resulting in destructive floods if the river is dammed by the rockslide and the dam fails. Our observations suggest that the occurrence of a slope failure during an exceptional rainfall is rather unlikely, and that the coupled risk of flood due to a slope collapse may be overestimated.

[49] Finally, we showed that rockfall occurrence is correlated with accelerations of the rockslide, the displacement rate being delayed by a few days relative to rockfall activity, and decreases more slowly to its mean value after about one month, compared to only 5 days for rockfall activity triggered by rainfall. This correlation is likely indirect, due to the influence of precipitation on both slope displacement and rockfall activity. Our interpretation is that rainfall immediately triggers rockfalls and also produces an acceleration of the rockslide displacement which lasts longer than triggered rockfalls due to inertial effects.

[50] **Acknowledgments.** We acknowledge CETE for providing displacement and meteorological data. METEO FRANCE, LTHE laboratory, and METEO VIZILLE also provided meteorological data, and François Thouvenot provided the Sismalp earthquake catalog. This research was supported by the European Commission under grant TRIGS-043251, by "Pôle Grenoblois d'Etudes et de Recherches pour la Prévention des Risques Naturels," and by French "Agence Nationale pour la Recherche" and "Institut des Sciences de l'Univers." We thank Pascal Lacroix and Jean-Robert Grasso for useful discussions. This work could not have been possible without the help from many technicians, engineers, students, and researchers from LGIT: we are grateful to Rémi Bethoux, Glenn Cougoulat, Sophie Cravoisier, Fabrice Doré, Jean-Robert Grasso, Armand Mariscal, Yves Orengo, Pascal Lacroix, Catherine Pequegnat, Sandrine Roussel, Laura Sanchez, Mohamed Tahir, Lucile Tatard, and Christophe Voisin for helping with installation and maintenance of the seismic network and data processing. We also thank Mauri McSaveney and an anonymous reviewer for their careful reading and for interesting suggestions, which helped improve

the quality of the manuscript. Finally, we thank the editor who carefully read the manuscript and proposed corrections to improve the English.

References

Alfonsi, P. (1997), Relation entre les paramètres hydrologiques et la vitesse dans les glissements de terrains: Exemples de La Clapière et de Séchilienne, *Rev. Fr. Geotech.*, *79*, 3–12.

Almendros, J., J. M. Ibáñez, G. Alguacil, and E. Del Pezzo (1999), Array analysis using circular-wave-front geometry: An application to locate the nearby seismo-volcanic source, *Geophys. J. Int.*, *136*, 159–170.

Amitrano, D., J. R. Grasso, and G. Senfaute (2005), Seismic precursory patterns before a cliff collapse and critical point phenomena, *Geophys. Res. Lett.*, *32*, L08314, doi:10.1029/2004GL022270.

Brocher, T. M. (2003), Detonation charge size versus coda magnitude relations in California and Nevada, *Bull. Seismol. Soc. Am.*, *93*, 2089–2105, doi:10.1785/0120020185.

Brodsky, E. E., E. Gordeev, and H. Kanamori (2003), Landslide basal friction as measured by seismic waves, *Geophys. Res. Lett.*, *30*(24), 2236, doi:10.1029/2003GL018485.

Caine, N. (1980), Rainfall intensity-duration control of shallow landslides and debris flows, *Geogr. Ann., Ser. A*, *62*, 23–27.

Chleborad, A. F., R. L. Baum, and J. W. Godt (2006), Rainfall thresholds for forecasting landslides in the Seattle, Washington, area: Exceedance and probability, *U.S. Geol. Surv. Open File Rep.*, *2006-1064*.

Crozier, M. J., and R. J. Eyles (1980), Assessing the probability of rapid mass movement, in *Proceedings of Third Australia-New Zealand Conference on Geomechanics*, edited by N. Z. Geomech. Soc., *Proc. Tech. Groups N. Z. Inst. Eng.*, *6*, 247–251.

Del Gaudio, V., S. Coccia, J. Wasowski, M. Gallipoli, and M. Mucciarelli (2008), Detection of directivity in seismic site response from microtremor spectral analysis, *Nat. Hazards Earth Syst. Sci.*, *8*, 751–762.

Deparis, J., D. Jongmans, F. Cotton, L. Baillet, F. Thouvenot, and D. Hantz (2008), Analysis of rock-fall seismograms in the western Alps, *Bull. Seismol. Soc. Am.*, *98*, 1781–1796.

Duranthon, J.-P., and L. Effendiantz (2004), The unstable "Ruines de Séchilienne" slope: State of site activity and presentation of the new remote-monitoring management system, *Bull. Lab. Ponts Chaussees*, *252*, 29–48.

Duranthon, J.-P., L. Effendiantz, M. Memier, and H. Previtali (2003), Apport des méthodes topographiques et topométriques au suivi du versant rocheux instable des "Ruines" de Séchilienne, *Rev. XYZ*, *94*, 31–38.

Effendiantz, L., and J.-P. Duranthon (2002), Risques majeur d'éboulement des Ruines de Séchilienne Point des mesures de suivi et de surveillance du site de 1985 au 31 Mars 2002, LRPC Rhône-Alpes, CETE de Lyon, Lyon, France.

Evrard, H., T. Gouin, A. Benoit, and J.-P. Duranthon (1990), Séchilienne: Risques majeurs d'éboulements en masse: Point sur la surveillance du site, *Bull. Liaison Lab. Ponts Chaussees*, *165*, 7–16

Frayssines, M., and D. Hantz (2006), Failure mechanisms and triggering factors in calcareous cliffs of the Subalpine Ranges (French Alps), *Eng. Geol.*, *86*, 256–270.

Giraud, A., L. Rochet, and P. Antoine (1990), Processes of slope failure in crystallophyllian formations, *Eng. Geol.*, *29*, 241–253.

Glade, T., M. Crozier, and P. Smith (2000), Applying probability determination to refine landslide-triggering rainfall threshold using an empirical antecedent daily rainfall model, *Pure Appl. Geophys.*, *157*, 1059–1079.

Guglielmi, Y., J. Vengeon, C. Bertrand, J. Mudry, J. Follacci, and A. Giraud (2002), Hydrogeochemistry: An investigation tool to evaluate infiltration into large moving rock masses (case study of La Clapière and Séchilienne alpine landslides), *Bull. Eng. Geol. Environ.*, *61*, 311–324.

Guzzetti, F., S. Peruccacci, M. Rossi, and C. P. Stark (2007), Rainfall thresholds for the initiation of landslides in central and southern Europe, *Meteorol. Atmos. Phys.*, *98*, 239–267, doi:10.1007/s00703-007-0262-7.

Harrington, R. M., and E. E. Brodsky (2007), Volcanic hybrid earthquakes that are brittle-failure events, *Geophys. Res. Lett.*, *34*, L06308, doi:10.1029/2006GL028714.

Helmstetter, A., L. Sanchez, S. Garambois, J. Grasso, F. Doré, Y. Orengo, J. Duranthon, P. Pothérat, and J. Kasperski (2008), Multidisciplinary monitoring of a huge rocky landslide (Séchilienne, the Alps, France), *Eos Trans. AGU*, *89*(53), Fall Meet. Suppl., Abstract H51F-0899.

Kasperski, J. (2008), Confrontation des données de terrain et de l'imagerie multi-sources pour la compréhension de la dynamique des mouvements de versants, Ph.D. thesis, 268 pp., Univ. Claude Bernard-Lyon I, Villeurbanne, France.

Lemaître, F., J.-C. Duranthon, and L. Effendiantz (2004), L'utilisation du radar au sol pour la surveillance des mouvements de terrain, *Bull. Lab. Ponts Chaussees*, *249*, 19–34.

Le Roux, O., S. Schwartz, J. F. Gamond, D. Jongmans, D. Bourles, R. Braucher, W. Mahaney, J. Carcaillet, and L. Leanni (2009), CRE dating on the head scarp of a major landslide (Séchilienne, French Alps), age constraints on Holocene kinematics, *Earth Planet. Sci. Lett.*, *280*, 236–245.

McSaveney, M. J. (2002), Recent rockfalls and rock avalanches in Mount Cook National Park, New Zealand, in *Catastrophic Landslides: Effects, Occurrence, and Mechanisms*, edited by S. G. Evans and J. V. DeGraff, *Rev. Eng. Geol.*, *15*, 35–70.

McSaveney, M. J., and G. Downes (2002), Application of landslide seismology to some New Zealand rock avalanches, in *Landslides*, edited by J. Rybář, J. Stemberk, and P. Wagner, pp. 649–654, A. A. Balkema, Lisse, Netherlands.

Méric, O., S. Garambois, D. Jongmans, M. Wathelet, J. L. Chatelain, and J. M. Vengeon (2005), Application of geophysical methods for the investigation of the large gravitational mass movement of Séchilienne, France, *Can. Geotech. J.*, *42*, 1105–1115.

Montjuvent, G., and J. Winistorfer (1980), Glaciations quaternaires dans les Alpes Franco-Suisses et leur piedmont, *Geol. Alp.*, *56*, 251–282.

Norris, R. D. (1994), Seismicity of rockfalls and avalanches at three cascade range volcanoes: Implications for seismic detection of hazardous mass movements, *Bull. Seismol. Soc. Am.*, *84*, 1925–1939.

Panet, M. (2000), Expertise relative aux risques d'éboulement du versant des Ruines de Séchilienne, 24 pp., Préfecture de l'Isère, Grenoble, France.

Pothérat, P., and P. Alfonsi (2001), Les mouvements de versant de Séchilienne (Isère): Prise en compte de l'héritage structural pour leur simulation numérique, *Rev. Fr. Geotech.*, *95*, 117–131.

Roth, M., M. Dietrich, L. H. Blikra, and I. Lecomte (2006), Seismic monitoring of the unstable rock slope site at Åknes, Norway, in *19th Annual Symposium on the Application of Geophysics to Engineering and Environmental Problems (SAGEEP)*, edited by J. Gamey, pp. 184–192, Environ. and Eng. Geophys. Soc., Denver, Colo.

Spillmann, T., H. Maurer, A. G. Green, B. Heincke, H. Willenberg, and S. Husen (2007), Microseismic investigation of an unstable mountain slope in the Swiss Alps, *J. Geophys. Res.*, *112*, B07301, doi:10.1029/2006JB004723.

Thouvenot, F., J. Fréchet, L. Jenatton, and J.-F. Gamond (2003), The Belledonne Border Fault: Identification of an active seismic strike-slip fault in the western Alps, *Geophys. J. Int.*, *155*, 174–192.

Vengeon, J.-M., A. Giraud, P. Antoine, and L. Rochet (1999), Contribution à l'analyse de la déformation et de la rupture des grands versants rocheux en terrain cristallophyllien, *Can. Geotech. J.*, *36*, 1123–1136, doi:10.1139/cgj-36-6-1123.

Weiss, J. (1997), The role of the attenuation on acoustic emission amplitude distributions and *b*-values, *Bull. Seismol. Soc. Am.*, *87*, 1362–1367.

S. Garambois and A. Helmstetter, Laboratoire de Géophysique Interne et Tectonophysique, Université Joseph Fourier, CNRS, F-38041 Grenoble, France. (stephane.garambois@ujf-grenoble.fr; ahelmste@obs.ujf-grenoble.fr)